# Multiline 3D beamforming using micro-beamformed datasets for pediatric transesophageal echocardiography

Bera, D.; Raghunathan, S.B.; Chen, C.; Chen, Z.; Pertijs, M.A.P.; Verweij, M.D.; Daeichin, V.; Vos, H.J.; van der Steen, A.F.W.; de Jong, N.

**DOI**
10.1088/1361-6560/aab45e

**Publication date**
2018

**Document Version**
Accepted author manuscript

**Published in**
Physics in Medicine and Biology

# Multiline 3D beamforming using micro-beamformed datasets for pediatric transesophageal echocardiography

D. Bera[1], S. B. Raghunathan[2], C. Chen[3], Z. Chen[3], M.A.P. Pertijs[3], M.D. Verweij[2], V. Daeichin[2], H.J. Vos[1,2], A.F.W. van der Steen[1,2], N. de Jong[1,2], J.G. Bosch[1]
1 Department of Biomedical Engineering, Thoraxcenter, Erasmus MC, Rotterdam, The Netherlands
2 Department of Acoustic Wavefield Imaging, Delft University of Technology, Delft, The Netherlands
3 Electronic Instrumentation Laboratory, Delft University of Technology, Delft, The Netherlands

**Abstract: Until now, no matrix transducer has been realized for 3D transesophageal echocardiography (TEE) in pediatric patients. In 3D TEE with a matrix transducer, the biggest challenges are to connect a large number of elements to a standard ultrasound system, and to achieve a high volume rate (>200 Hz). To address these issues, we have recently developed a prototype miniaturized matrix transducer for pediatric patients with micro-beamforming and a small central transmitter. In this paper we propose two multiline parallel 3D beamforming techniques (μBF25 and μBF169) using the micro-beamformed datasets from 25 and 169 transmit events to achieve volume rates of 300 Hz and 44 Hz, respectively. Both the realizations use angle-weighted combination of the neighboring overlapping sub-volumes to avoid artifacts due to sharp intensity changes introduced by parallel beamforming. In simulation, the image quality in terms of the width of the point spread function (PSF), lateral shift invariance and mean clutter level for volumes produced by μBF25 and μBF169 are similar to the idealized beamforming using a conventional single-line acquisition with a fully-sampled matrix transducer (FS4k, 4225 transmit events). For completeness, we also investigated a 9 transmit-scheme (3×3) that allows even higher frame rates but found worse B-mode image quality with our probe. The simulations were experimentally verified by acquiring the μBF datasets from the prototype using a Verasonics V1 research ultrasound system. For both μBF169 and μBF25, the experimental PSFs were similar to the simulated PSFs, but in the experimental PSFs, the clutter level was ~10 dB higher. Results indicate that the proposed multiline 3D beamforming techniques with the prototype matrix transducer are promising candidates for real-time pediatric 3D TEE.**

**Keywords: Transesophageal echocardiography, pediatric TEE, matrix transducer, sub-array beamforming, parallel beamforming, volumetric imaging**

## 1. Introduction

### 1.1 Pediatric Transesophageal Echocardiography

Transesophageal Echocardiography (TEE) allows imaging of the heart from the esophagus, avoiding artifacts due to the lungs and the rib cage. A few years ago, a MicroMulti TEE (μTEE) [1] probe was introduced primarily for neonatal and pediatric applications [2]. The μTEE probe has shown to be successful in imaging infant patients with weights as low as 1.7 kg without any major difficulties [1], [2]. Additionally, due to its small size, the μTEE probe is very useful for monitoring adults undergoing catheter ablation for atrial fibrillation and atrial septal defects, without sedation [3], [4]. This probe can also be used for diagnosing hemodynamically unstable patients in intensive care units [5]. Even though the μTEE probe is very useful for real-time 2D imaging, it is incapable of performing real-time 3D imaging of the heart.

Recently, real-time three dimensional TEE (3D TEE) has become an indispensable diagnostic modality to examine the complex 3D cardiac anatomy and function [6], [7]. In addition to that, 3D TEE helps to guide

and monitor surgical and catheter-based interventions [8], [9]. At present, for 3D TEE in adults, a number of matrix TEE probes (Philips X7-2t [10], Siemens V5M TEE [11], GE 6VT-D [12]) are commercially available. These matrix TEE probes are suitable for real-time acquisition and live 3D display in adults. However, they are much larger in size than a µTEE probe and therefore cannot be used in pediatric patients. Also, without full anesthesia, the 3D TEE probes are not suitable for long-term monitoring in adults, due to patient discomfort. Additionally, pediatric patients in general have higher heart rates than adults, and to accurately image the moving cardiac structures, a higher volume rate is required. Although a volume rate >40 Hz is already sufficient for B-mode imaging, for advanced applications such as 3D particle image velocimetry or speckle tracking higher volume rates (~200 Hz) are required. Moreover, to measure electromechanical wave propagation through the Purkinje fibers and myocardium and the resulting transient motion of the heart wall, a frame rate higher than 200 Hz is mandatory [13], [14]. Hence, if a matrix TEE probe with similar dimensions as the µTEE probe with the capability of high frame rate volume imaging would be available, it could be used both as a pediatric probe as well as an adult probe for long-term monitoring.

### 1.2 Challenges in real-time 3D imaging

There are two major challenges in real-time 3D ultrasound imaging using a matrix transducer. The first challenge is to achieve a sufficiently high frame rate. The second challenge is the enormous number of transducer elements and the limited number of transmit/receive channels to connect these with the ultrasound system. Both challenges are interrelated.

The first challenge has generally been addressed from the early days of 3D imaging [15], [16] through parallel beamforming. In classical ultrasound, one image line is constructed from one transmit, along a narrow transmit beam. In volumetric imaging, where thousands of lines are needed for one volume, this is prohibitive. The attainable frame rate can be increased considerably by using wide (either plane or diverging) transmit beams and reconstructing multiple receive scanlines in parallel from each transmission [17]–[21].

To address the second challenge, sparse arrays, multiplexing and micro-beamforming (or sub-array beamforming) have been proposed. Sparse arrays [22] are known to produce poor image quality, and multiplexing is in direct conflict with the first challenge. 3D imaging with micro-beamforming [19], [21], [22] can result in good images while reducing the receive channel count considerably. The principle of micro-beamforming is to subdivide the array into groups of $N$ neighboring elements and to achieve pre-steering by applying micro-delays to the element signals before summing them, thus producing a single partially beamformed or micro-beamformed RF signal (µBRF) per group. This step is typically performed within a front-end ASIC, and reduction in channel count by a factor $N$ is thereby achieved. An external ultrasound scanner then receives the micro-beamformed RF signals from all sub-arrays and performs a delay-and-sum (DAS) beamforming to achieve full dynamic receive focusing (DRF).

Recently, a high frame rate 3D imaging scheme using diverging transmit waves with a GE 6VT-D TEE probe comprising of micro-beamforming capabilities has been proposed in [25]. In that work, it was shown that with only 9 diverging transmit waves (3×3 in lateral and elevation directions) and receive pre-steering co-aligned with the transmit beam directions, a volume with 70°×70° sector can be produced at volume rates of ~600 Hz with an image quality suitable for Tissue Doppler Imaging, but not for the best B-mode images. In this paper we will also investigate the suitability of such an imaging scheme with 3×3 beams for a prototype matrix transducer described below.

### 1.3 Parallel beamforming

Parallel beamforming was first proposed in [15] to achieve high frame rate volumetric imaging. Although the parallel beamforming technique enables imaging at high frame rate, it produces images with compromised image quality. In parallel beamforming, the scanlines from one transmission show higher correlation among themselves than with scanlines from neighboring transmissions. This results in an imaging artifact: sharp intensity changes at the transition between the scanlines from different transmissions. We refer to these artifacts as *crossover artifacts*. Several approaches have been proposed [17]–[19] to overcome the latter two limitations of parallel beamforming for 2D imaging using both linear array and phased array transducers. It has been shown that these crossover artifacts can be avoided by synthesizing transmit beams through interpolation of the unfocused received signals prior to the beamforming [17]. For a phased array, spatial compounding of the beamformed scanlines from multiple transmissions has been proposed to suppress these artifacts [19]. Thus, it is possible to avoid the crossover artifacts by combining the beamformed scanlines from neighboring transmissions.

### 1.4 Prototype miniaturized matrix TEE transducer

We have recently designed and realized a matrix TEE transducer [26] with small dimensions suitable for pediatric 3D TEE and/or for long-term monitoring in adults. This design has the capability of parallel beamforming for high frame rate 3D imaging. It features a receive aperture similar to the 2D µTEE ($5 \times 5$ $mm^2$), and a very small central transmit aperture, capable of generating broad transmit beams suitable for parallel beamforming. It is equipped with an ASIC for micro-beamforming to reduce the receive channel count and achieve a pre-steering capability.

None of the previously proposed parallel beamforming approaches is directly suitable for this prototype matrix transducer, given its transmitter-receiver layout and pre-steering capability. Therefore, the aim of this paper is the design and assessment of a suitable parallel beamforming scheme that can achieve good image quality and sufficiently high volume rate (>200 Hz) with this type of transducer.

### 1.5 Proposed 3D beamforming schemes

The prototype transducer has a small transmit aperture, therefore it can suitably generate wide transmit beams. The wide transmit beams help in achieving high frame rate imaging using parallel beamforming but lead to reduced image quality. Furthermore, the receive pre-steering is limited to only 25 fixed directions in 3D space. In practice, this means that for each acquisition we have to choose the direction of pre-steering from the 25 directions and transmit a wide beam in an appropriate direction. We call this a transmit-receive event (tx-rx event). Hence, to achieve good-quality 3D images at a high frame rate, we need to find a 3D beamforming scheme that requires a minimal number of tx-rx events and also minimizes the image artifacts. In this paper, we investigated four parallel-beamforming schemes utilizing the high frame rate capabilities of the prototype transducer, and compare their performance in terms of image quality and frame rate. The first scheme requires 25 tx-rx events per volume, the second one 169 tx-rx events, and the third and the fourth scheme require only 9 tx-rx events per volume. To suppress sharp intensity changes in the proposed scheme, the scanlines for the final volume are produced by linearly combining the scanlines of the sub-volumes from neighboring tx-rx events. We refer to this scheme as *sub-volume crossfading*. As a result, all the beamforming schemes avoid the imaging artifacts due to the sharp intensity changes while switching from one transmission to the other. All of the proposed schemes can produce volume images at a high frame rate (>40 Hz) by utilizing the broad transmissions and the limited number of pre-steering directions. We compare the image quality and frame rate of the proposed beamforming schemes with an ideal but slow 3D beamforming technique (4225 scanlines; one

tx-rx event per scanline). The ideal 3D beamforming is performed in simulation using a hypothetical fully sampled (FS) matrix transducer of the same size and transmitter-receiver layout as the prototype transducer.

### 1.6 Structure of the paper

A detailed description of the prototype matrix transducer, the two proposed 3D beamforming techniques and the idealized 3D beamforming technique are presented in Section 2. Section 2 also describes the setup of numerical simulations and experimental validation with an ultrasound research scanner. Section 3 compares the image quality of the 3D beamforming schemes in simulations and experiments. The paper ends with a discussion of the results of the beamforming schemes as well as future work regarding real-time 3D TEE using the prototype matrix transducer.

## 2. Materials and Methods

### 2.1 Description of the prototype matrix transducer

We have recently designed and realized a prototype miniaturized matrix TEE transducer [26] with dimensions similar to a 2D µTEE probe: a $5 \times 5$ mm$^2$ aperture consisting of $32 \times 32$ individual PZT elements. The element pitch is 150 µm and the center frequency is 5 MHz. The transducer array is constructed by dicing a bulk piezo-electrical material (3203HD, CTS Corporation, Albuquerque, MN, USA) with a dicing kerf width of 20 µm. The PZT stack is mounted directly on top of a front-end ASIC using the PZT-on-CMOS integration scheme described in [27]. For simplification of the electronics design, the transmit and receive elements are completely separated electrically.

Figure 1 shows the layout of transmit and receive elements. The transducer has a very small transmit aperture area ($1.2 \times 1.2$ mm$^2$), consisting of $8 \times 8$ elements at the center. These transmit elements are wired out directly to an ultrasound scanner. The transmit array is capable of steering to any direction in 3D space, but due to the small aperture size, the natural focus is shallow. Hence, the array cannot focus at a relevant depth; it produces wide transmit beams suitable for parallel beamforming, selectively steered in 3D space. The 864 receive elements are connected directly to the front-end ASIC for micro-beamforming [26]. The receive elements are divided into 96 sub-arrays of $3 \times 3$ elements. The signals from each element of a sub-array are delayed with analog delays and summed by a micro-beamformer in the front-end ASIC. The micro-beamformers reduce the number of cables by a factor of 9. Thus, the 864 receive elements of the prototype are funneled into 96 sub-arrays, and their signals are fed to the receive channels of an external ultrasound scanner. In this paper, the output signals of all sub-arrays for one tx-rx event are referred to as a µBRF dataset. The analog delays for elements in a sub-array can be programmed from 30 ns up to 180 ns in steps of 30 ns. These analog delays can steer an individual sub-array to angles of 0°, ±17°, and ±37° in both lateral and elevation directions. Thus, by using the micro-beamforming, the receiver can be pre-steered to 25 fixed directions in the 3D space.

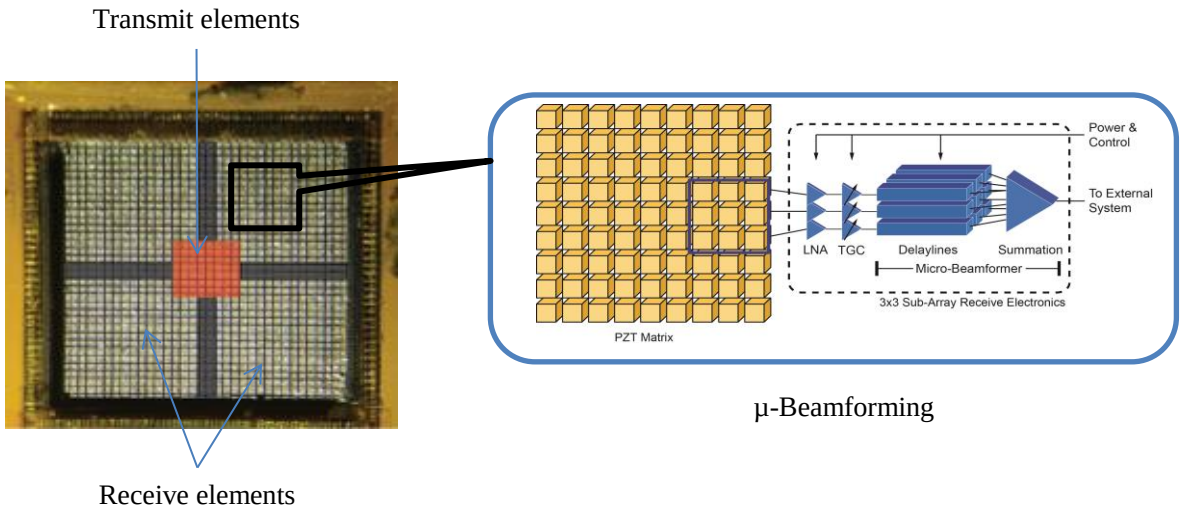


Figure 1: Layout of the custom designed pediatric 3D TEE transducer [26]

## 2.2 Parallel beamforming with pre-steering

The 3D parallel beamforming schemes are performed in three steps. In the first step, the receive sub-arrays are pre-steered to one of the 25 fixed directions. A diverging transmit beam is steered to the same direction or to an adjacent direction, and the 96-channel µBRF dataset is acquired. In the second step, DAS beamforming is applied to the µBRF dataset to produce a sub-volume of 3D beamformed scanlines. To cover a desired volume, these two steps are repeated several times to generate overlapping 3D sub-volumes, each from a different tx-rx event. In the third step, each scanline in the final volume is produced by selecting and/or combining scanlines from the sub-volumes reconstructed using the µBRF datasets of the neighboring tx-rx events.

The pre-steered received beams from a single sub-array of the prototype have an opening angle of ~50°. Although it is possible to reconstruct a full volume using only one acquired µBRF dataset, the image intensity will be the best in the proximity of the pre-steering direction. Additionally, such a single-event µBRF contains grating lobes due to large pitch (1.5λ) between sub-arrays. Hence, to minimize the amplitude variation in the final volume and to suppress grating lobes, transmissions are steered to the angles close to the pre-steering directions. A single sub-volume consisting of only a pre-defined set of scanlines is produced using a µBRF dataset received from a single tx-rx event. Figure 2 shows an example of parallel beamforming along with receive pre-steering. In this figure, the regions correspond to the 25 receive pre-steering directions. Figure 2(a) depicts one tx-rx event and its beamformed scanlines. In this example, the receive sub-arrays are pre-steered to an angle $(\theta, \varphi)$ = (0°,17°), where $\theta$ is the angle in lateral direction ($X$), and $\varphi$ is the angle in elevation direction ($Y$). A diverging transmit beam is then steered to the same angle $(\theta, \varphi)$ = (0°,17°). After that, the µBRF dataset of this tx-rx event is used to reconstruct the RF scanlines of the region, as highlighted in Figure 2(a). To reconstruct a volume covering ±45°, both in lateral and elevation directions, the scanlines for all the 25 regions are reconstructed. This switching from one tx-rx event to the other for reconstructing individual regions leads to image artifacts in the form of sharp intensity changes and speckle discontinuities at the region borders, which was not covered in earlier methods of parallel beamforming in presence of micro-beamforming [25].

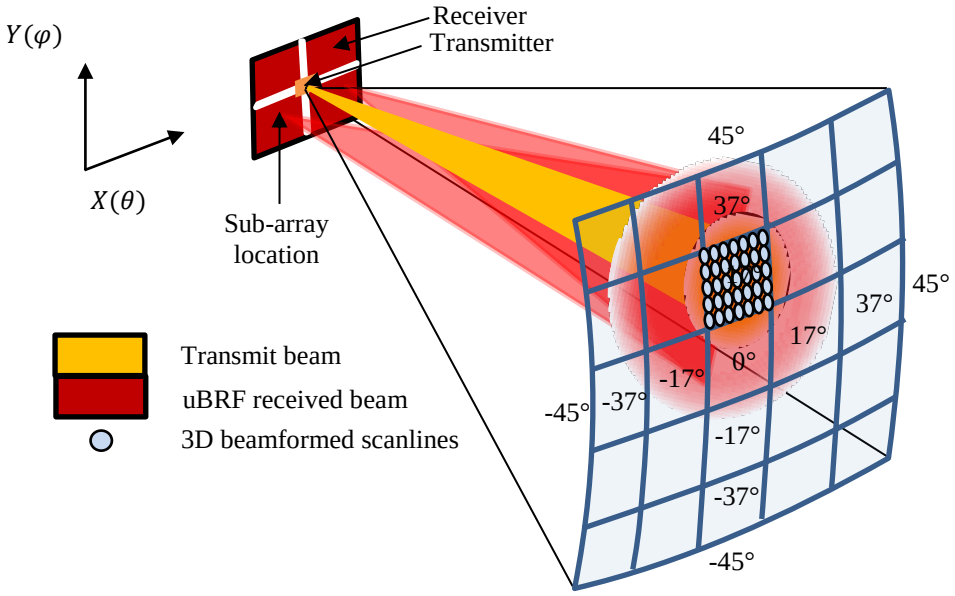


(a)

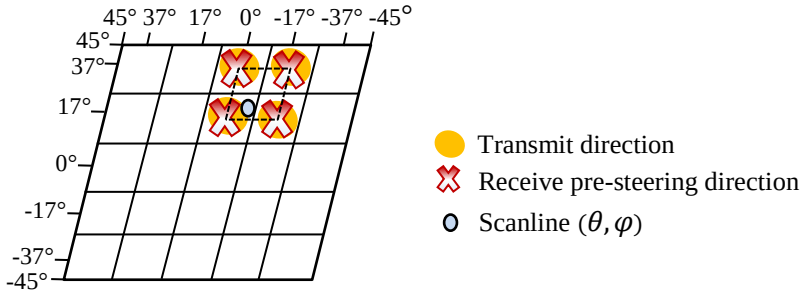


(b)

Figure 2: (a) Diverging transmit beam, µBRF received beam, 3D beamformed scanlines and 25 pre-steering regions lying on a spherical surface. (b) Illustration of µBF25: Diverging transmit beams steered to angles aligned with the pre-steering angles. Scanlines of the intermediate angles/regions are reconstructed using neighboring tx-rx events. All the scanlines within the dotted rectangle are built by a linear combination from the same four tx-rx events (-17<= $\boldsymbol{\theta}$ <=0;17<= $\boldsymbol{\varphi}$ <=37)

## 2.3 Proposed parallel beamforming with 25 tx-rx events (µBF25)

To minimize the image artifacts due to µBRF switching, we combined the scanlines produced from the µBRF dataset of the neighboring directions, as shown in Figure 2(b). Hence, each scanline at an angle $(\theta, \varphi)$ in the final volume $V_f$ was produced as a weighted sum of the scanlines for that angle from the sub-volumes of adjacent tx-rx events:

$$V_f(\theta,\varphi) = \{\sum_m w(\theta-\theta_m, \varphi-\varphi_m)\cdot V_m(\theta,\varphi): |\theta-\theta_m| \le \delta, |\varphi-\varphi_m| \le \delta\} \quad (1)$$
$$\text{with } \sum_m w(\theta-\theta_m, \varphi-\varphi_m) = 1, m \in M \text{ and } M \subset [1,25],$$

where $V_m(\theta, \varphi)$ is the scanline corresponding to the $m^{th}$ tx-rx event steered to $(\theta_m, \varphi_m)$. The weight $w$ is constructed using coefficients from a Hanning window and assigned to the scanline at $(\theta, \varphi)$ based on its proximity to the direction $(\theta_m, \varphi_m)$. $\delta$ is chosen such that for each scanline in $V_f$, M contains a set of maximum four neighboring tx-rx events from the available 25 tx-rx events. Thus, the µBF25 technique performs a weighted sum of corresponding scanlines from the adjacent tx-rx events to produce a volume with minimized image artifacts. Figure 2(b) illustrates how all the scanlines within the dotted rectangle are built as a linear combination from the same four tx-rx events.

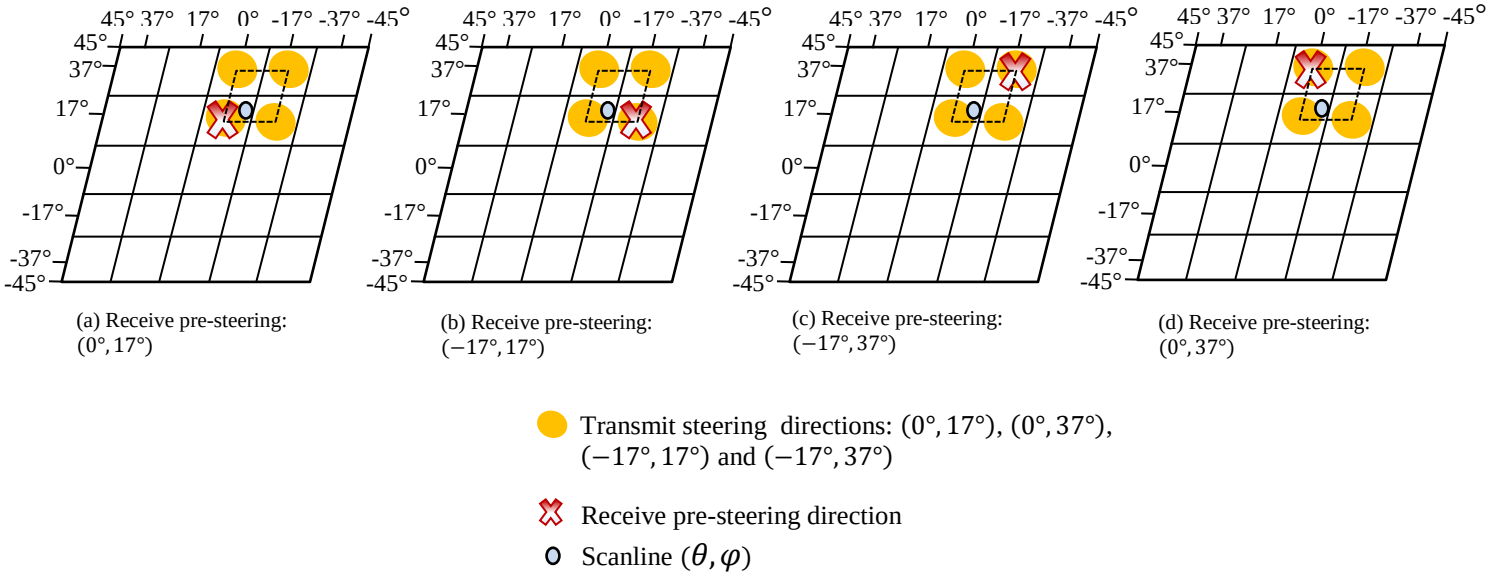


Figure 3: Illustration of µBF169: Diverging transmit beams steered to a pre-steering direction and to three neighboring directions while using the same receive pre-steering. Scanlines of the intermediate angles/regions are reconstructed using all 16 neighboring tx-rx events

2.4 Proposed parallel beamforming with 169 tx-rx events (µBF169)

As mentioned, the pre-steered receive beams from a single sub-array have an opening angle of ~53°, and the transmit beam had an opening angle of ~17° (at -3 dB level). Hence, a pre-steered receive beam overlaps not only with the transmission to its own pre-steering direction but also with the transmissions to the neighboring directions. These overlaps between the pre-steering receive beam and the neighboring transmissions imply that those tx-rx events contain relevant information of scatterers within that zone. To exploit that additional information, we propose an alternative 3D beamforming technique with 169 tx-rx events to achieve improved image quality. Accordingly, each scanline at an angle $(\theta, \varphi)$ in the final volume $V_f$ was produced using scanlines from all the adjacent tx-rx events, as shown in Figure 3, using

$$V_f(\theta, \varphi) = \left\{ \begin{matrix} \sum_m w(\Delta\theta_m^t, \Delta\varphi_m^t, \Delta\theta_m^r, \Delta\varphi_m^r) \cdot V_m(\theta, \varphi) : |\Delta\theta_m^t|, |\Delta\theta_m^r| \leq \delta \\ and\ |\Delta\varphi_m^t|, |\Delta\varphi_m^r| \leq \delta \end{matrix} \right\} \quad (2)$$

$$\text{with } \Delta\theta_m^t = \theta - \theta_m^t, \Delta\varphi_m^t = \varphi - \varphi_m^t, \Delta\theta_m^r = \theta - \theta_m^r \text{ and } \Delta\varphi_m^r = \varphi - \varphi_m^r$$

$$\text{and } \sum_m w(\Delta\theta_m^t, \Delta\varphi_m^t, \Delta\theta_m^r, \Delta\varphi_m^r) = 1, m \in N \text{ and } N \subset [1,169]$$

where $V_m(\theta, \varphi)$ is the scanline corresponding to the $m^{\text{th}}$ tx-rx event. For the $m^{\text{th}}$ tx-rx event, the angle of transmission $(\theta_m^t, \varphi_m^t)$ and the angle of receive pre-steering $(\theta_m^r, \varphi_m^r)$, together determine $\delta$, i.e. the size of the region of reconstruction. For a scanline at $(\theta, \varphi)$, the weight $w$ is determined based on the deviation from $(\theta_m^t, \varphi_m^t)$ and $(\theta_m^r, \varphi_m^r)$. For each scanline, $N$ contains a set of 16 neighboring tx-rx events from the total 169 tx-rx events.

### 2.5 Proposed parallel beamforming with 9 tx-rx events (μBF9)

To achieve higher frame rate than μBF25, we explored possible parallel beamforming using less than 25 tx-rx events. Because of the wide opening angle of the transmit beams and the receive beams from the sub-arrays, it is possible to cover an entire volume (of 90°×90° viewing angle) with only 9 tx-rx events and achieve a volume rate even higher than μBF25. For volume reconstruction with 9 tx-rx events, considering the transmit direction to be the same as pre-steering direction, we chose the transmit steering and receive pre-steering angles to the central direction and either to ±17° or ±37° in both lateral and elevation directions. Both in the proposed μBF9 with ±17° (μBF9n) and μBF9 with ±37° (μBF9w), to produce the final volume, angle weighted linear combination similar to μBF25 was applied to avoid the image artifacts.

### 2.6 Ideal DAS with fully-sampled matrix transducer (FS4k)

To compare the performance of the proposed beamforming techniques with an ideal DAS 3D beamforming, an idealized FS matrix transducer was simulated with all settings similar to the prototype transducer, such as the pitch, center frequency and the number and configuration of transmit and receive elements (Table 1). All transmit and receive elements in the FS transducer, however, were individually addressable (no micro-beamforming, all elements wired out). To achieve the best image quality with the given transmit and receive aperture, for each scanline in the volume one tx-rx event was used, where both transmit and receive were steered in the exact direction of the scanline, with the narrowest possible transmit beam. For such a small receive aperture size (5×5 $mm^2$, with natural focus at 20 mm), DRF will not make any difference in the image quality beyond 20 mm. Therefore, in receive, instead of DRF, we used fixed focusing at 40 mm depth. To reconstruct 65×65 scanlines, 4225 tx-rx events were needed. This 'ideal' beamforming was therefore named FS4k.

For all the 3D beamforming schemes, the final volume in Cartesian coordinates was produced by performing envelope detection, logarithmic compression and scan conversion on the volume in $(r, \theta, \varphi)$ domain (where r represents depth). The performance of the beamforming schemes was then compared for image quality.

For an imaging depth of 10 cm (and thus a PRF of 7.5 kHz) and scan angle of ±45° in lateral and elevation directions, FS4k will yield a volume rate of 1.78 Hz. For the same imaging depth, μBF25 can achieve a volume rate of 300 Hz. Both μBF9 methods can achieve a volume rate of 833.4 Hz, which is even higher than μBF25. The proposed μBF169 requires about 7 times more transmissions than μBF25 and thus can achieve a volume rate of 44.4 Hz.

### 2.7 Simulation and experimental setup

The proposed 3D beamforming schemes were examined using simulations in FieldII [26] and verified by post-processing of μBRF datasets, acquired from the prototype transducer with a commercial research ultrasound system. The simulations were performed with a model of our prototype matrix transducer using similar properties [12]. The image quality was determined based on the following criteria: clutter

levels, uniformity of intensity distribution and width of point spread function (PSF) in lateral and elevation directions.

2.7.1 Simulation setup

The FieldII simulations of the proposed techniques were carried out with the transducer parameters and imaging parameters as shown in Table 1. The impulse response of the transducer was modelled as a 2 cycle sinusoid. The transducer excitation was a 3 cycle sinusoid tone burst. The image quality was determined by simulating different sets of point scatterers located at several positions in 3D space. The widths of PSFs were determined by simulating five point scatterers on the C-plane at 20 mm depth as shown in Figure 4. One of the five scatterers was placed at the center, the others were placed at extreme positions (±8.5 mm) in *X* and *Y* direction.

The clutter level and uniformity of intensity distribution were examined by placing a scatterer at 65 consecutive positions on a 20 mm C-plane, with its lateral position ranging between -16 mm and 16 mm. for each scatterer position, an entire volume was reconstructed to determine the clutter level and uniformity of the intensity distribution.

2.7.2 Measures of image quality in simulation

*A. Width of PSF:* For all the methods, the lateral and elevation PSFs were exactly the same because of the symmetric layout of the transducer elements in both directions. Hence, for all the volumes produced in simulations, we report only the width of the PSFs in the lateral direction from the response of the point scatterers in the central position. In simulation, to estimate the performance of the proposed 3D beamforming techniques, the widths of PSFs in the lateral and elevation directions were computed at -6 dB and at -20 dB and compared with FS4k.

*B. Shift invariance:* For multiline reconstruction, uniformity of the intensity distribution over 3D space may be compromised (as shown by the imaging artifact mentioned in 2.2). In general, this is referred to as spatial shift variance or translation (in) variance: if the probe is moved with respect to the scatterers, the image should only translate, and not change in any other way. To estimate uniformity of the intensity distribution, we determined the normalized maximum intensity of the individual PSFs (corresponding to each of the 65 scatterer positions) with respect to the maximum intensity of the central scatterer position.

*C. Clutter level:* Clutter is an artifact in ultrasound images that appears as diffuse echoes superimposed on the received signals of interest. In our PSF measurement, we considered all echoes outside of the -20 dB edge of the main lobe as clutter. For each volume reconstruction technique, the mean clutter level was calculated by taking an average of the clutter level for each 65 volumes produced from the 65 positions of a single point scatterer between -20 mm to +20 mm in the lateral direction.

Table 1: Parameters of simulations

| | Parameters | Value |
|---|---|---|
| Transducer | Center frequency | 4.5 MHz |
| | Number of transmit elements | 64 |
| | Number of receive elements | 864 |
| | Pitch | 150 µm |
| | Number of receive sub-arrays | 96 |
| | Receive sub-array pitch | 450 µm |
| Simulation parameters | Pulse duration | 0.6 µs |
| | Apodization | Box-car |
| | Sampling frequency | 100 MHz |
| | Transmit focus | -1.2 mm |
| | Receive focus | 40 mm |
| | Imaging depth | 60 mm |
| | Transmit steering angles | 0°, ±17° and ±37° in lateral and elevation and all 65×65 angles for FS4k |
| 3D reconstruction | Number of scanlines | 65×65 |
| | Scan angle | ±45° |

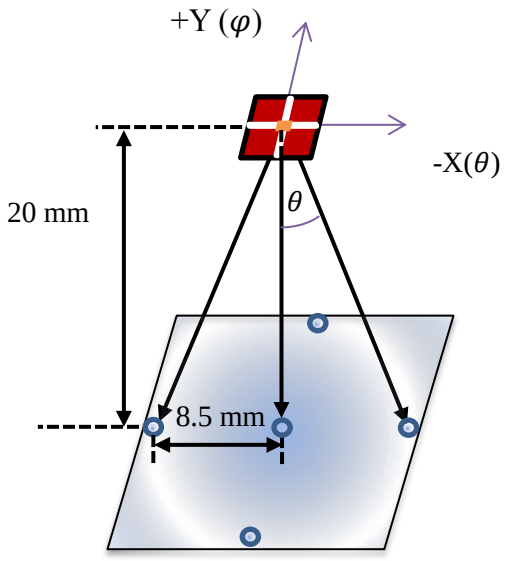


Figure 4: Positions of the five point scatterers in 3D space for measuring PSF width

2.7.3 Experimental setup

To investigate the performance of the proposed 3D beamforming schemes, data were acquired by connecting the prototype matrix transducer [12] to a Verasonics V1 ultrasound system (Verasonics Inc. Kirkland, Washington, USA). The experiment was done with seven point scatterers (six steel balls and one needle) in water, placed on a C-plane at a depth of 35 mm. For each tx-rx event, the delays

corresponding to a pre-steering angle were loaded to the ASIC, using an external FPGA. A diverging transmit beam was then steered to the desired direction and the µBRF dataset received by the sub-arrays was acquired. The diverging transmit beams were produced by placing the transmission focus behind the transducer at -1.2 mm, and the transducer excitation was a 3 cycle sinusoid tone burst. Appropriate transmit delays for focusing and steering were generated by the Verasonics and applied to the individual transmit elements of the prototype transducer. For each tx-rx event, the µBRF dataset was acquired with fixed gain settings, at 18 MHz sampling rate and stored for post-processing. Before 3D beamforming, the µBRF datasets were filtered with a band-pass filter of 100% bandwidth with 4.5 MHz center frequency.

## 3. Results

### 3.1 Simulation results

#### 3.1.1 Volume reconstructed using a single tx-rx event

Image intensity of a full volume reconstructed using a single µBRF dataset acquired for a specific tx-rx event will be the best in the proximity of the transmit and pre-steering direction. Figure 5 shows the 2D slices (located at 0° elevation angle) of the two simulated polar volume images reconstructed for the five point scatterers (shown in Figure 4) using µBRF datasets acquired from two different tx-rx events. For both of the two tx-rx events, transmissions were steered to (0°,0°). However, the pre-steering directions for the two volume images were (-37°,0°) and (0°,0°). The images are shown in polar coordinates for easier interpretation of sidelobes and clutter. The point scatterer at -8.5 mm (at -23° in Figure 5) in the lateral direction is brighter in Figure 5(b) than in Figure 5(c). Furthermore, in Figure 5(b), the intensity of the central scatterer was highest compared to the other scatterers that were away from the center. Additionally, in Figure 5(b) the central scatterer appeared to be asymmetric, and the scatterer at +23° was completely obscured by the clutter from the scatterer at -23°. This clutter was caused by the grating lobes produced due to the pre-steering to (-37°, 0°). Thus, Figure 5 shows that for a given tx-rx event only a defined 3D region close to the transmit and pre-steering direction has high intensity; all the other regions in the 3D space suffer from poor intensity and clutter. This uneven intensity distribution and clutter suggest that only the defined illuminated sub-volume (closer to the transmit and pre-steering direction) should be reconstructed from each tx-rx event; and thus, multiple tx-rx events should be used to reconstruct the final volume to achieve better image quality.

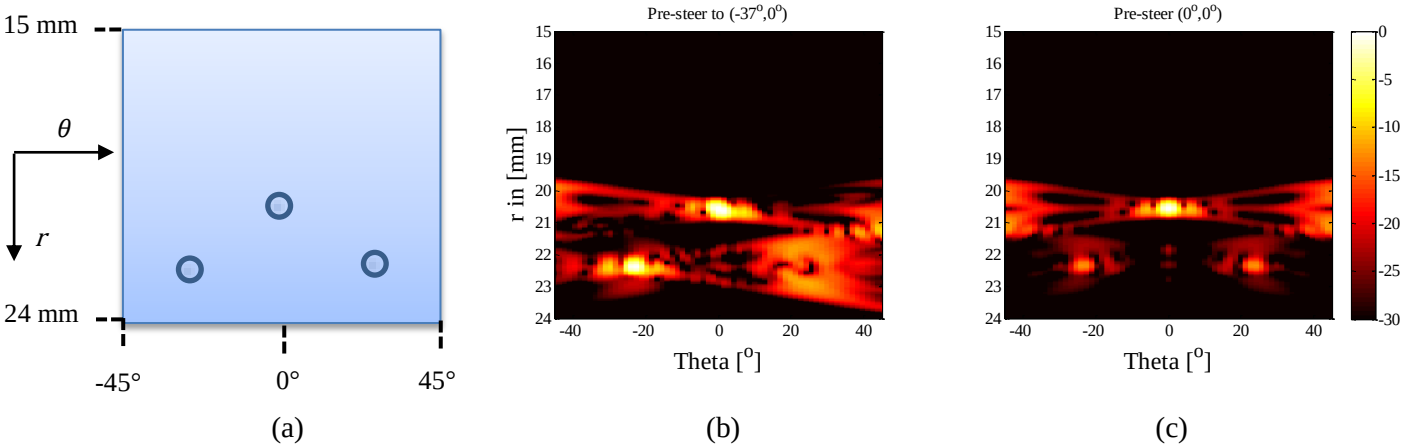


Figure 5: (a) Schematic of the position of the three point scatterers in polar space. 2D slices at 0° elevation angle of polar volumes reconstructed from two tx-rx events (b) pre-steered to (-37,0) and (c) pre-steered to (0,0)

### 3.1.2 Volume reconstructed using simple parallel beamforming

For each tx-rx event, the quality of the volume image in terms of intensity is the best close to the pre-steering direction. Therefore, as described in Section 2.2, a complete volume ranging ±45° in both lateral and elevation directions was produced using 25 tx-rx events. Figure 6 shows polar volume images sliced into two 2D planes located at 0° lateral angle and at 0° elevation angle. The volumes were reconstructed with point scatterers located at the same positions as in Figure 5. These images contain sharp boundaries introduced by the transition from one tx-rx event to the other at 9° and 23°. The image artifacts caused by the sharp boundaries are indicated by arrows. Since these artifacts are not acceptable in clinical practice, we consider combining overlapped µBRF datasets in the following sections.

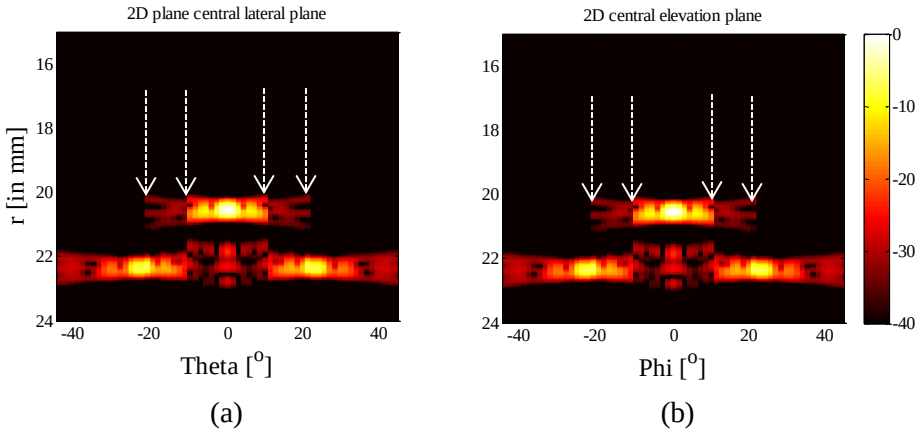


Figure 6: 2D polar images with simple parallel beamforming (hard boundaries). (a) Central lateral plane and (b) central elevation plane.

### 3.1.3 Comparison of width of PSF for µBF25, µBF169, µBF9 and FS4k

Figure 7 shows 2D polar planes sliced from polar volume images at 0° elevation angle for µBF25, µBF169, µBF9n, µBF9w, and FS4k. Unlike the images produced using simple parallel beamforming (in Figure 6), in all the five images produced by µBF25, µBF169, two µBF9 and FS4k, we do not see the crossover artifacts described before. However, µBF9 with both ±17° and ±37° produce images degraded with off-axis energy. In Figure 7(c), for µBF9n, off-axis energy for the central scatterer is visible at extreme angles. In Figure 7(d), for µBF9w, the scatterers at ±23° are less intense and degraded by off-axis energies. Hence, both the µBF9 techniques produced images with inferior image quality compared to µBF25 and µBF169. For quantitative comparison between the PSFs of these 3D beamforming schemes, the angular intensity profile of the central point scatterer along the lateral direction at 20 mm depth and 0° elevation angle are plotted in Figure 8. It can be observed that the angular widths at -6 dB for all the five methods are almost the same (~4°). However, µBF169 produced slightly lower (~2 dB) sidelobes and µBF9w produced slightly higher sidelobes than all other beamforming methods. The lateral angular width of the PSF at -20 dB for µBF9n [Figure 7(c)] is similar to µBF25 [Figure 7(a)]. However, at wider angles, the PSF for µBF9n shows the highest clutter level among all other beamforming. The lateral angular width of the PSF at -20 dB for µBF25 is ~2° wider than both µBF169 [Figure 7(b)] and FS4k [Figure 7(e)]. Thus, considering the widths of the PSFs µBF169 performs better than all other proposed high frame rate beamforming methods.

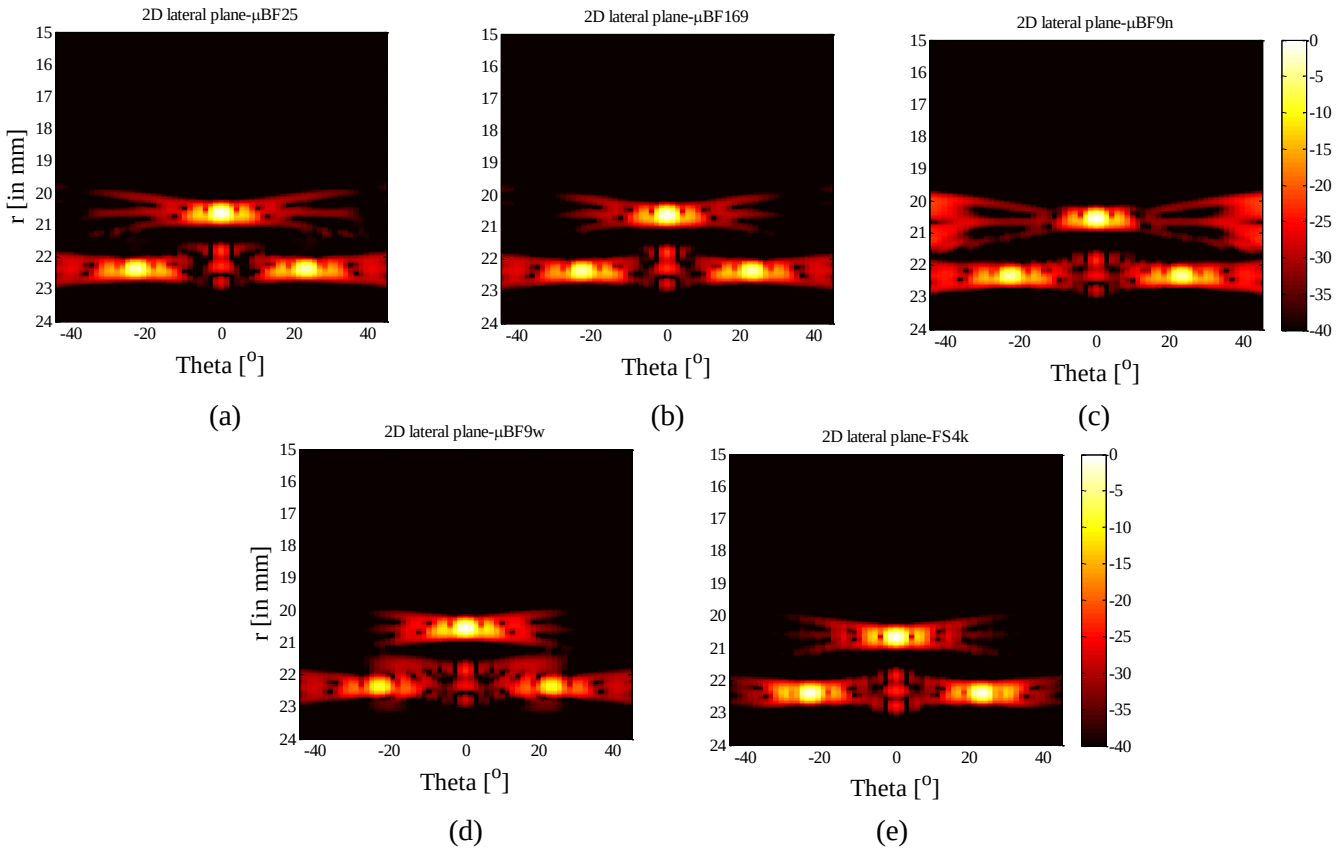


Figure 7: Polar images for 2D lateral plane of 3 point scatterers using (a) µBF25, (b) µBF169, (c) µBF9n, (d) µBF9w and (e) FS4k.

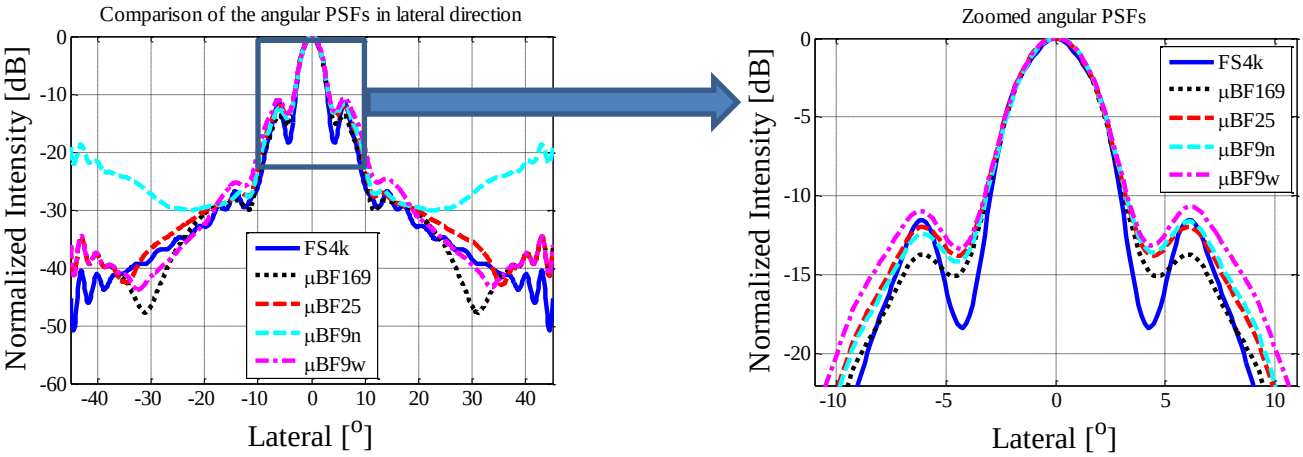


Figure 8: Simulated PSFs of uBF25, uBF169, µBF9n, µBF9w and FS4k

### 3.1.4 Shift invariance

Figure 9 shows the maximum intensity for the 65 point scatterer locations with respect to the maximum intensity of the central scatterer position located on the C-plane at 20 mm and simulated using µBF25, µBF169 and FS4k. For FS4k, the normalized maximum intensities of the scatterers were almost uniform (with a gradual decrease with increase in angle and minor variations). However, for both µBF25 and µBF169 sharp intensity drops were visible at four locations. A drop of ~4 dB was observed for the point scatterer located at ±25°, and a drop of ~3 dB was observed for the point scatterer at ±9°. In addition to that, a drop of ~7 dB was observed for the point scatterer at ±45°. For both µBF25 and µBF169, the point scatterers at ±17° and ±37° on the fixed C-plane had similar intensities compared to FS4k. In terms of uniformity of intensity distribution, both µBF25 and µBF169 performed relatively poorer than FS4k. However, there were no significant differences observed between the performance of µBF25 and µBF169.

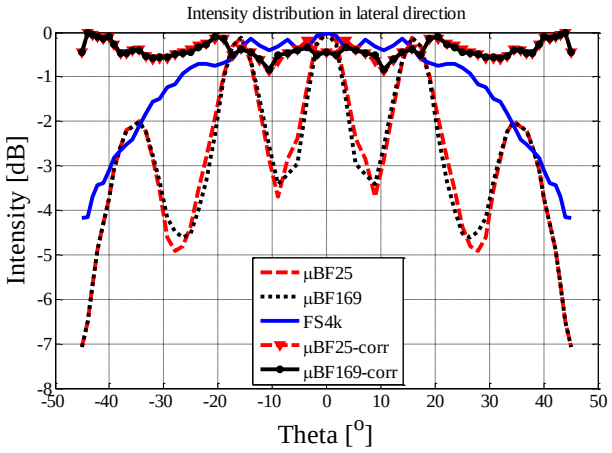


Figure 9: Uniformity of intensity distribution for 65 point scatterer positions along lateral direction.

The intensity drops for µBF25 and µBF169 were present due to the fixed receive pre-steering and transmit directions causing lower sensitivity at the interposed angles. It is evident that the intensity drops for µBF9n and µBF9w were more severe, as the angular gap between consecutive tx-rx directions was even larger than µBF25 and µBF169. For a clearer representation, we did not show those intensity profiles in Figure 9. To compensate for the intensity variation, both in µBF25 and µBF169, the beamformed RF lines were weighted with the inverse of the intensity profiles. The weights for the polar volume data were computed using a linear interpolation on the weights for the 65 lateral positions. From Figure 9, it can be observed that after the compensation, the corrected intensity profiles for both µBF25 and µBF169 (intensity plots marked with triangles and circles) were uniform. The slight variation in the final normalized intensity levels could be due to a minor numerical imprecision while interpolating the weights for the polar volume data. Similar to µBF25 and µBF169, the required intensity compensation was also applied to correct the intensity drops in µBF9n and µBF9w. In practice, this compensation will lower the signal to noise ratio (SNR) for the lines that needed a relatively large gain compensation.

For the analysis of the lateral shift invariance, Figure 10 shows five contour plots obtained after stacking the intensity compensated PSFs for 65 lateral positions using all the five beamforming schemes. In such a plot, a perfect lateral shift invariant beamforming technique should yield a uniform diagonal structure. These plots show that among the five techniques, as expected, FS4k [Figure 10(e)] is the best in terms of shift invariance and both µBF9n [Figure 10(c)] and µBF9w [Figure 10(d)] are worse. For both µBF9n and µBF9w, the point scatterers around the center (in between -20° and 20°) show larger shift variances. Both

µBF25 [Figure 10(a)] and µBF169 [Figure 10(b)] had larger shift variances for the point scatterers at the interposed angles (at ±9° and ±25°) due to the fixed receive pre-steering and transmit directions. However, µBF169 is slightly less lateral shift variant than µBF25. Although intensity compensation yielded uniform maximum intensities at different positions, it increased the clutter levels at the interposed angles. However, as expected from the previous results (shown in Figure 8), all the three techniques were almost equally lateral shift invariant when considered until -20 dB.

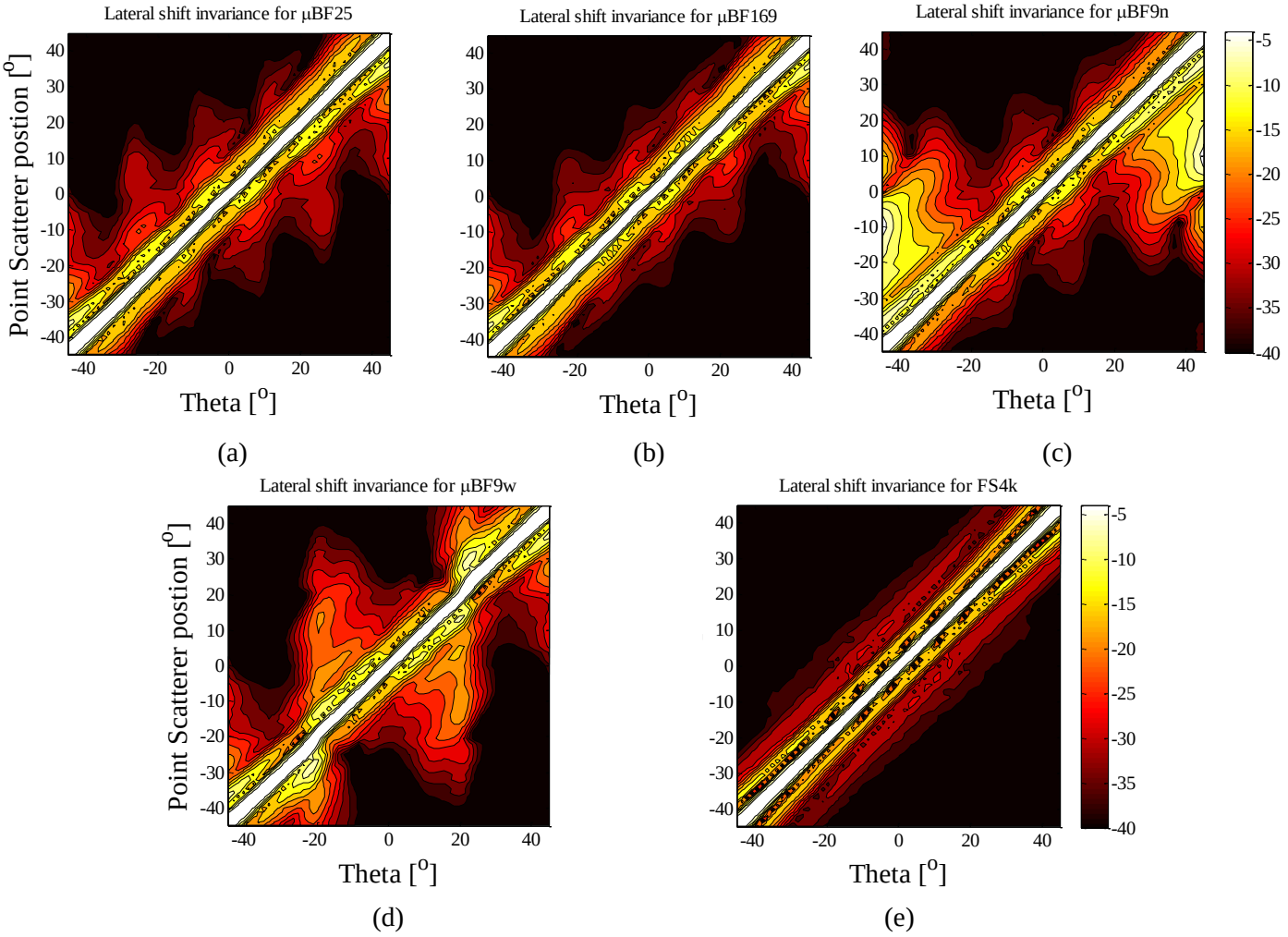


Figure 10: Contour plots of stacked PSFs for 65 lateral positions using (a) µBF25, (b) µBF169, (c) µBF9n, (d) µBF9w and (e) FS4k

### 3.1.5 Clutter levels

Figure 11 shows the mean clutter levels for the 65 point scatters located on the C-plane at 20 mm and simulated using µBF25, µBF169 and FS4k. From the figure, it can be observed that the profile of the mean clutter levels was quite uniform for FS4k. However, for both µBF25 and µBF169, the profiles of the mean clutter levels had valleys at the pre-steering angles and peaks at the interposed angles (±9°, ±25°). The mean clutter levels for µBF25 were ~2 dB higher than µBF169. It can also be observed that the average of the mean clutter levels over different lateral positions for both µBF25 and µBF169 was ~-77 dB. The average of the mean clutter levels for FS4k was ~2 dB lower than µBF25, µBF169. It is obvious from

Figure 10 that the mean clutter level for the two µBF9 methods will be higher than others, therefore, we have not shown them in Figure 11.

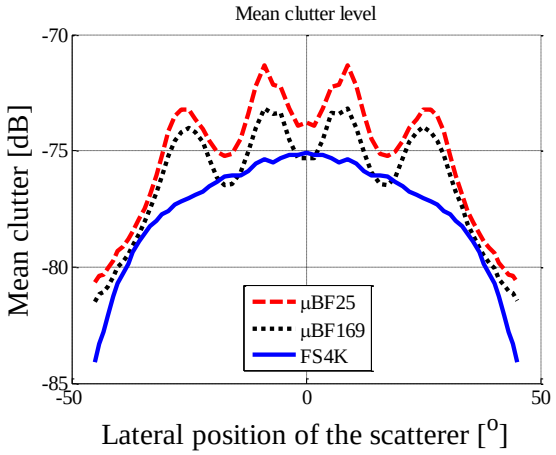


Figure 11: Mean clutter level for 65 scatterer positions along lateral direction.

3.2 Experimental results

3.2.1 Volume rendered image

Figure 12(a) and Figure 12(b) show the positions of the 7 point scatterers (six steel balls and one needle) of the phantom, Figure 12(c) and Figure 12(d) show the corresponding volume rendered images using µBF25 and µBF169 of this phantom placed on a C-plane at 35 mm with 40 dB dynamic range. In both Figure 12(c) and (d), the positions of the point scatterers accurately matched with the actual positions of the scatterers. However, from Figure 12, it can be observed that the clutter level in volume rendered image using µBF25 is slightly higher than the image using µBF169 [indicated by arrows in Figure 12(c) and (d)]. The needle (scatterer 4) did not have a steel ball on the top, so in the rendered images it appeared with less intensity. In the rendered images, for each scatterer, one main lobe and four sidelobes (in both lateral and elevation directions) were observed. The skewed appearance of the sidelobes was caused by few non-working receive sub-arrays in the prototype transducer. We have observed the same pattern of the sidelobes in simulation with the absence of those non-working sub-arrays. Similar to the simulation results, in experimental results, µBF25 produce volume images with similar appearance as µBF169 but with somewhat higher clutter levels.

3.2.2 Comparison between the widths of simulated and measured PSF

Figure 13(a) and Figure 13(b) show the PSFs in lateral and elevation directions for the central scatterer of µBF25 and µBF169 from the phantom measurement and the simulation of µBF169. From these figures, it can be observed that the widths of the main lobe at -6 dB, in both lateral and elevation directions from the measurement are ~4°, which are the same as the widths from the simulation (as shown in Figure 8). However, for lateral direction, the sidelobe levels in both µBF169 and µBF25 are ~2 dB higher in the measurement than in the simulation. Additionally, the lateral PSF for µBF25 from the experiment has 3 dB higher clutter levels than µBF169 at -30° and 33°. Whereas, the elevational PSF for µBF25 from the experiment has 3 dB higher clutter levels than µBF169 at -30° and 28°. The clutter levels in the experiment are on average ~10 dB higher than simulation. The asymmetry of the PSFs and the higher clutter levels in the experiment were due to the non-working receive sub-arrays in the prototype transducer.

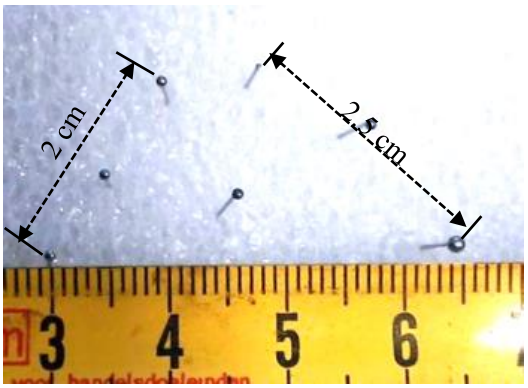


(a)

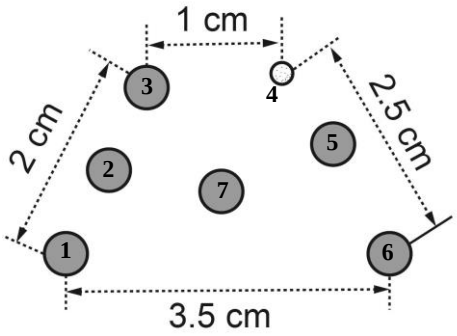


(b)

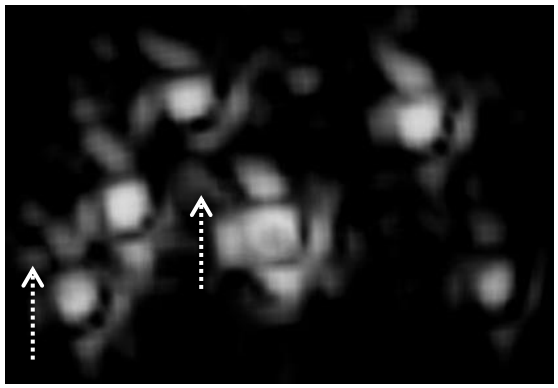

(c)

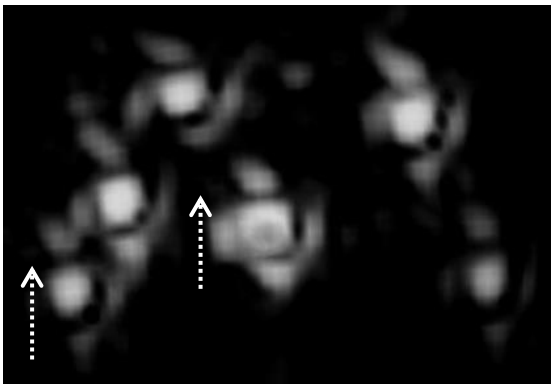

(d)

Figure 12: (a) The seven point scatterers used in the experiment, (b) the pattern of the 7 point scatterers including six steel balls (gray circles) and 1 needle (white circle), (c) volume rendered image using µBF25 and (d) volume rendered image using µBF169

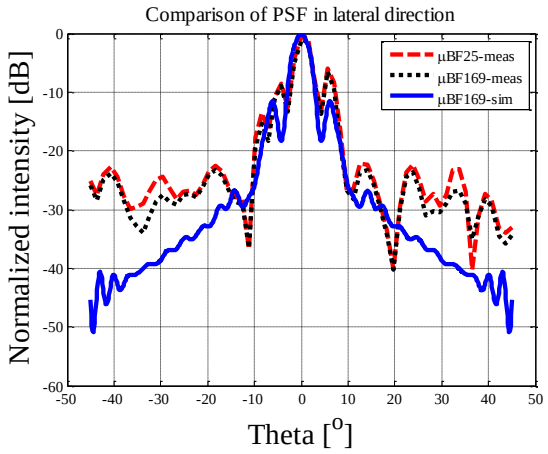


(a)

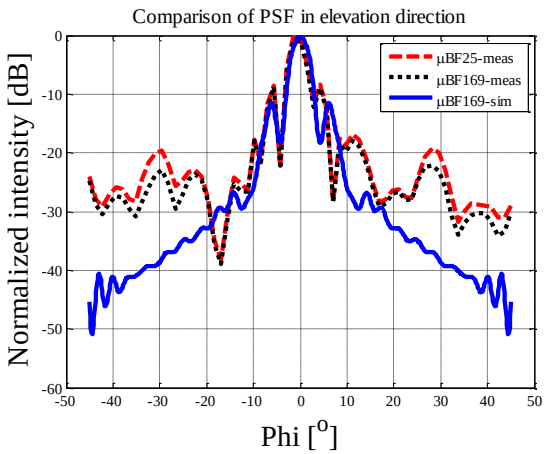


(b)

Figure 13: PSFs of µBF25 and µBF169 for the central scatterer in (a) lateral direction and (b) elevation direction from the experiment and compared with simulated µBF169

## 4. Discussion

The purpose of the present research was to develop a 3D beamforming technique to produce high-quality volume images at a higher volume rate (>80 Hz) than conventional 3D ultrasound imaging, using the designed prototype matrix transducer. Because of the specific architecture of the prototype transducer, existing parallel beamforming techniques were not directly suitable for it. Therefore, in this study, we proposed two multiline 3D beamforming schemes, µBF25 and µBF169, that utilize the capabilities of the prototype transducer. In simulation, the proposed schemes yielded volumes with image quality similar to the volume using conventional single line acquisition with a fully sampled matrix. This was validated experimentally. The schemes were capable of producing high-quality volume images at a higher frame rate than conventional single line acquisition on the prototype miniaturized matrix transducer.

The receive micro-beamformers allowed to pre-steer to 25 fixed angles in 3D. Hence, for a tx-rx event steered to a certain angle, only a specific sub-volume around that angle was beamformed. To avoid the crossover artifacts, we use sub-volume crossfading. In the µBF25 scheme, overlapping sub-volumes using co-aligned tx-rx events were linearly combined to produce the final volume. In the µBF169 scheme, in addition to the tx-rx events used in µBF25, sub-volumes from non-aligned tx-rx events were also combined to utilize the overlap between the pre-steered receive beams and the wide transmit beams. The widths of the PSFs at -6 dB and -20 dB in lateral and elevation directions for µBF25 and µBF169 were very similar to the widths of the PSFs of FS4k that would be obtained by full-aperture, line-based volumetric imaging. This was expected as the -6dB width of the PSF primarily depends on the size of the aperture of the transducer.

In simulation, the normalized intensity distribution showed that the intensity was highest at the direction of transmit and receive steering and dropped at the borders of the transmit and receive zones. This is caused by the combined transmit-receive beamprofile, and it was corrected using the inverse of the normalized intensity profile as a gain/weighting factor for the beamformed RF lines. However, these gains also increased the noise level with the same factors. The lateral shift invariance test showed that after the intensity compensation both µBF25 and µBF169 performed as good as FS4k considering upto -20 dB. However, both the methods had higher intensity variation than FS4k between -20 dB and -40 dB. We performed the shift invariance test and intensity compensation only in the lateral direction, as the same intensity profile is expected in the elevation direction.

To achieve higher volume rate than µBF25, we also tested the performance of two beamforming schemes using only 9 tx-rx events (µBF9, 3×3 beams). The quantified PSFs for the two µBF9 methods showed degraded image quality due to larger intensity drops and a higher clutter level. Moreover, the lateral shift invariance test showed that µBF9 with both ±17° and ±37° produced volume images with larger variance. Hence, for the designed prototype, the proposed µBF9 methods were not suitable for producing volume images with acceptable B-mode image quality. Note that this conclusion may seem different from that drawn in [25], which also uses a 3×3 scheme with a TEE probe with pre-steering capabilities. However, the data in [25] is Doppler-processed to obtain tissue velocity, which is in principle insensitive to amplitude variances, provided that the SNR is sufficient. Our current study aims at B-mode imaging, and therefore the two conclusions do not contradict each other.

The main lobes of the PSFs for µBF169 and µBF25 (shown in Figure 13) closely match with the PSF for µBF169 in simulation, showing the accuracy of the performance of the transducer. However, the sidelobes observed in the measured PSFs were higher than in simulation and also asymmetric (slightly tilted). The differences in the sidelobes are due to the specific distribution of few non-working sub-arrays in the prototype transducer. We think this effect will not be visible with a transducer in which all sub-arrays are functional. The clutter levels of the PSFs in the experiments were higher than in simulation primarily due to the following reasons: the non-working sub-groups, noise introduced by the electronics of the prototype transducer and the external ultrasound system.

From the simulation and experimental results of µBF25 and µBF169, one could conclude that combining more sub-volumes from different combinations of tx-rx provides only a minor improvement in the image quality. However, it should be noted that for µBF169, it is also important to have overlaps between the transmit beams and the pre-steered receive beams. A narrow transmit beam will have a lesser overlap, leading to almost no effect in the final volume, even after combining the overlapped sub-volumes. On the other hand, increasing transmit opening angle will reduce the penetration depth causing reduction of the SNR at higher imaging depth. Accordingly, choosing an optimum transmit opening angle for the best achievable image quality is subject to further research.

From these results, it can be concluded that µBF25 produces similar image quality as µBF169 with 7 times higher frame rate, except for a minor increase in clutter. Therefore, to produce a high-quality image at higher frame rate using our prototype, µBF25 is preferred over µBF169.

There are a few limitations that apply to this study. The 3D beamforming technique was examined only with static pin phantoms. In future research, we will verify the effects of moving tissue on the proposed beamforming techniques, e.g. by imaging dynamic heart phantoms similar to what has been described in [28], [29] followed by *in vivo* imaging in animals and humans. In addition, our study has not investigated other image quality measures, such as axial resolution, contrast ratio (CR), contrast-to-noise ratio (CNR), signal-to-noise ratio (SNR) etc. The axial resolution is mainly determined by the pulse characteristics. As we have used the same pulse characteristics for all the beamforming techniques, we expect no differences in axial resolution among them. The other important image quality parameters (the CR and CNR) have not been evaluated during this research. The clutter levels of the PSFs in experiments were at the most ~10 dB higher than in simulation and only present at extreme angles. Therefore, this difference in clutter level is not expected to provide any significant differences in CR and CTR. In µBF169 we are combining sub-volumes from larger number of neighboring tx-rx events than µBF25. Therefore, µBF169 might help in improving the resulting SNR. In addition to that, for µBF169, the SNR might also be improved because of the suppression of the off-axis energies. Additionally, to improve the uniformity of intensity distribution, the effect of interposed angle transmissions (i.e., at angles of ±9° and ±25°) should be investigated to find if this would provide more optimal uniformity. Although interposed transmissions may provide more uniform overall intensity, the receive sensitivity will be reduced by a few dB in those directions due to the limited pre-steering capability of the ASIC of the prototype transducer.

## 5. Conclusion

We have proposed and implemented two multiline 3D beamforming schemes to produce volumes with good image quality at a maximum volume rate of 300 Hz using a prototype miniaturized matrix transducer with micro-beamformer suitable for pediatric Transesophageal Echocardiography (TEE) and for continuous monitoring in adults. In simulation, the image quality (width of PSFs, lateral shift invariance and clutter level) of the volumes produced by the proposed techniques were similar to the volume using conventional single line acquisition with a hypothetical, idealized fully-sampled matrix transducer of the same size and transmitter-receiver layout as the prototype transducer. The proposed µBF25 can produce volume images at 169 times higher frame rate than the ideal single-line acquisition method. In addition to that, because of the high volume rate (300 Hz) capability, µBF25 can be suitable for advanced clinical application such as 3D particle image velocimetry [30] or speckle tracking. The proposed µBF169 can produce volume images with good quality at a volume rate (>40 Hz) sufficient for B-mode imaging. The main lobe widths of the PSFs in both lateral and elevation direction from the experiment were ~4°, in good agreement with the simulated PSFs. From these results, we can conclude that the proposed 3D beamforming techniques are suitable for the prototype matrix transducer to produce a high-quality image at a high frame rate.

Acknowledgements

This work is part of the Open Technology Programme with project number 12405 which is (partly) financed by the Netherlands Organisation for Scientific Research (NWO). We like to thank Oldelft Ultrasound, Delft, the Netherlands for their valuable support in transducer manufacturing.

References

[1] S. C. Zyblewski *et al.*, "Initial Experience With a Miniaturized Multiplane Transesophageal Probe in Small Infants Undergoing Cardiac Operations," *Ann. Thorac. Surg.*, vol. 89, no. 6, pp. 1990–1994, 2010.

[2] K. Pushparajah, O. I. Miller, D. Rawlins, A. Barlow, K. Nugent, and J. M. Simpson, "Clinical application of a micro multiplane transoesophageal probe in congenital cardiac disease," *Cardiol. Young*, vol. 22, no. 2, pp. 170–7, 2012.

[3] S. Stec, B. Zaborska, M. Sikora-Frc, T. Kryski, and P. Kuakowski, "First experience with microprobe transoesophageal echocardiography in non-sedated adults undergoing atrial fibrillation ablation: Feasibility study and comparison with intracardiac echocardiography," *Europace*, vol. 13, no. 1, pp. 51–56, 2011.

[4] M. Taniguchi, T. Akagi, Y. Kijima, H. Ito, and S. Sano, "Transcatheter closure of a large atrial septal defect under microprobe transesophageal echocardiographic guidance," *Echocardiography*, vol. 29, no. 4, 2012.

[5] C. E. Wagner, J. S. Bick, B. H. Webster, J. H. Selby, and J. G. Byrne, "Use of a miniaturized transesophageal echocardiographic probe in the intensive care unit for diagnosis and treatment of a hemodynamically unstable patient after aortic valve replacement," *J. Cardiothorac. Vasc. Anesth.*, vol. 26, no. 1, pp. 95–97, 2012.

[6] P. M. Kapoor *et al.*, "An update on transesophageal echocardiography views 2016: 2D versus 3D tee views," *Ann. Card. Anaesth.*, vol. 19, no. Supplement, pp. S56–S72, 2016.

[7] M. Montealegre-Gallegos, F. Mahmood, K. Owais, P. Hess, J. S. Jainandunsing, and R. Matyal, "Cardiac Output Calculation and Three-Dimensional Echocardiography," *J. Cardiothorac. Vasc. Anesth.*, vol. 28, no. 3, pp. 547–550, 2014.

[8] L. H. Frank, A. Chelliah, and C. Sable, "Evaluation of a second-generation microtransesophageal echocardiography transducer and software.," *World J. Pediatr. Congenit. Heart Surg.*, vol. 5, no. 4, pp. 565–70, 2014.

[9] L. Sugeng *et al.*, "Real-Time Three-Dimensional Transesophageal Echocardiography in Valve Disease: Comparison With Surgical Findings and Evaluation of Prosthetic Valves," *J. Am. Soc. Echocardiogr.*, vol. 21, no. 12, pp. 1347–1354, 2008.

[10] I. S. Salgo, "Three-Dimensional Echocardiographic Technology," *Cardiol. Clin.*, vol. 25, no. 2, pp. 231–239, 2007.

[11] Siemens, "syngo fourSight TEE view." [Online]. Available: https://www.healthcare.siemens.com/ultrasound/options-and-upgrades/clinical-applications/syngo-foursight-tee-view. [Accessed: 25-Jul-2016].

[12] GE Healthcare, "Vivid ™ E9 XDclear ™," 2013.

[13] M. Pernot and E. E. Konofagou, "Electromechanical imaging of the myocardium at normal and pathological states," in *IEEE Ultrasonics Symposium*, 2005, vol. 2, pp. 1091–1094.

[14] J. Provost, W.-N. Lee, K. Fujikura, and E. E. Konofagou, "Imaging the electromechanical activity of the heart in vivo," *Proc. Natl. Acad. Sci. U. S. A.*, vol. 108, no. 21, pp. 8565–70, 2011.

[15] D. P. Shattuck, M. D. Weinshenker, S. W. Smith, and O. T. von Ramm, "Explososcan: a parallel processing technique for high speed ultrasound imaging with linear phased arrays," *J. Acoust. Soc. Am.*, vol. 75, no. 4, pp. 1273–1282, 1984.

[16] O. T. Von Ramm, S. W. Smith, and H. G. Pavy, "High-speed Ultrasound Volumetric Imaging System- Part II : Parallel Processing and Image Display," *IEEE Trans. Ultrason. Ferroelectr.*

*Freq. Control*, vol. 38, no. 2, pp. 100–108, 1991.

[17] T. Hergum, T. G. Bjåstad, K. Kristoffersen, and H. Torp, "Parallel Beamforming Using Synthetic Transmit Beams," *IEEE Trans. Ultrason. Ferroelectr. Freq. Control*, vol. 54, no. 2, pp. 271–280, 2007.

[18] L. Tong, A. Ramalli, R. Jasaityte, P. Tortoli, and J. D'Hooge, "Multi-Transmit Beam Forming for Fast Cardiac Imaging — Experimental Validation and In Vivo Application," vol. 33, no. 6, pp. 1205–1219, 2014.

[19] H. Hasegawa and H. Kanai, "High-frame-rate echocardiography using diverging transmit beams and parallel receive beamforming," *J. Med. Ultrason.*, vol. 38, no. 3, pp. 129–140, 2011.

[20] J. Provost *et al.*, "3D ultrafast ultrasound imaging in vivo.," *Phys. Med. Biol.*, vol. 59, no. 19, pp. L1–L13, 2014.

[21] P. Santos *et al.*, "Acoustic Output of Multi-Line Transmit Beamforming for Fast Cardiac Imaging," vol. 62, no. 7, pp. 1320–1330, 2015.

[22] A. Austeng and S. Holm, "Sparse 2-D arrays for 3-D phased array imaging - Design methods," *IEEE Trans. Ultrason. Ferroelectr. Freq. Control*, vol. 49, no. 8, pp. 1073–1086, 2002.

[23] B. Savord and R. Solomon, "Fully sampled matrix transducer for real time 3D ultrasonic imaging," in *IEEE Ultrasonics Symposium*, 2003, vol. 1, pp. 945–953.

[24] S. Blaak, C. T. Lancée, J. G. Bosch, C. Prins, A. F. W. Van Der Steen, and N. De Jong, "A matrix transducer for 3D transesophageal echocardiography with a separate transmit and receive subarray," in *IEEE Ultrasonics Symposium*, 2011, pp. 2341–2344.

[25] P. Santos, G. Haugen, L. Løvstakken, E. Samset, and J. D'hooge, "Diverging Wave Volumetric Imaging Using Subaperture Beamforming," *Ultrason. Ferroelectr. Freq. Control. IEEE Trans.*, vol. 63, no. 12, pp. 2114–2124, 2016.

[26] C. Chen *et al.*, "A Front-End ASIC With Receive Sub-array Beamforming Integrated With a 32 x 32 PZT Matrix Transducer for 3-D Transesophageal Echocardiography," *IEEE J. Solid-State Circuits*, vol. 63, no. 1, pp. 1–13, 2017.

[27] C. Chen *et al.*, "A Prototype PZT Matrix Transducer with Low-Power Integrated Receive ASIC for 3D Transesophageal Echocardiography," *IEEE Trans. Ultrason. Ferroelectr. Freq. Control*, vol. 63, no. 1, pp. 47–59, 2016.

[28] F. P. Li, M. Rajchl, J. Moore, and T. M. Peters, "A mitral annulus tracking approach for navigation of off-pump beating heart mitral valve repair," *Med. Phys.*, vol. 42, no. 1, pp. 456–468, 2015.

[29] P. W. Wood, P. H. Gibson, and H. Becher, "Three-dimensional echocardiography in a dynamic heart phantom: comparison of five different methods to measure chamber volume using a commercially available software," *Echo Res. Pract.*, vol. 1, no. 2, pp. 51–60, 2014.

[30] J. D. Voorneveld, D. Bera, A. F. W. van der Steen, N. de Jong, and J. G. Bosch, "Particle image velocimetry on simulated 3D ultrafast ultrasound from pediatric matrix TEE transducers," in *Proc. SPIE, Medical Imaging 2017*, 2016, vol. 10139, pp. 1–9.